Design of PWM-SMC Controller Using Linearized Model for Grid-Connected Inverter With *LCL* Filter

Han Li, Weimin Wu, *Member, IEEE*, Min Huang, Henry Shu-hung Chung, *Fellow, IEEE*, Marco Liserre, *Fellow, IEEE*, and Frede Blaabjerg, *Fellow, IEEE*

***Abstract*—Nowadays, various sliding-mode control (SMC) methods have been successfully applied to the digitally controlled grid-connected inverter (GCI) with an *LCL* filter. However, how to design the pulsewidth modulation based SMC (PWM-SMC) controller needs to be further explored, especially upon the large variation of the parameters drift and the delay issue. In this article, the essence of two classic SMC methods used in the power converter area is first analyzed in detail. Thus, a novel design of the PWM-SMC controller using a linearized model for the three-phase GCI with an *LCL* filter is proposed. Based on this, a three-loop step-by-step design of the PWM-SMC controller is developed, by using the closed-loop pole locations. A robust analysis against the parameters drift is also studied. In addition, a discrete state observer is adopted to reduce the number of sensors. Furthermore, a discussion between the proposed control strategy with the existing SMC methods and the full-state feedback controller is carried out. Finally, a 3-kW lab device designed on the dSPACE is constructed to verify the feasibility of the proposed strategy and the correctness of the theoretical analysis.**

***Index Terms*—Grid-connected inverter (GCI), *LCL*-filter, parameters drift, robust, sliding-mode control, stability analysis, state observer.**

I. Introduction

DUE to the environmental concerns and fossil energy crisis problems, in recent years, research works on the renewable energy grid-connected power generation technology have received extensive attention [1]. As the core component of the system, the grid-connected inverter (GCI) is charged with the task of injecting a high-quality current into the power grid in a stable and efficient way. For this purpose, a power filter (*L* or *LCL*) is often used to suppress the high-frequency harmonics generated by switching operations. Compared with the *L* filter, a third-order *LCL* filter has been widely adopted, owing to its better ability to attenuate the high-frequency harmonics with relatively smaller inductance [2]. However, it has an inherent resonant problem that may seriously deteriorate the stability of the whole system [3]–[5], especially when the grid distortion and parameters drift occur in GCI systems, resulting in a critical challenge in the current regulator design.

Nowadays, to improve the stability, many linear controllers combined with active damping methods have been applied to the *LCL*-filtered GCI [6]–[12]. Besides, various nonlinear controllers have been deeply studied, such as predictive controller [13]–[16], Lyapunov-function-based controller [17], passive-based controller [18]–[20], adaptive controller [21], [22], deadbeat controller [23]–[25], and sliding-mode control (SMC) controller [26]–[31]. As one of the nonlinear controllers, the SMC controller has attracted many interests, due to its strong robustness against system parameter uncertainties.

Currently, according to the switching mode, there are two kinds of SMC controllers for the *LCL*-filtered GCI. One is the hysteresis modulation based SMC (HM-SMC) [26]–[28], while the other is the pulsewidth modulation based SMC (PWM-SMC) [29]–[31].

In the HM-SMC methods, Komurcugil *et al*. [26] had proposed a new sliding surface function with a double-band hysteresis scheme, which can reduce the number of sensors and achieve good dynamic performance. Guzman *et al*. [27] had integrated the Kalman filter (KF) with the SMC controller for *LCL*-filtered inverters, using a reduced model to achieve high robustness against the *LCL* parameters drift. Also, Guzman *et al*. [28] had proposed a control algorithm in a natural frame based on SMC together with KF to obtain three decoupled controllers, which can provide the desired dynamics for the grid-injected current. However, the hysteresis modulation will cause the variable switching frequency, resulting in the difficulty of designing the output power filter. Besides, a high sampling frequency has to be adopted for the HM-SMC, increasing the implementation difficulty.

The PWM-SMC can realize the fixed switching frequency operation. Hao *et al.* [29] adopted the equivalent SMC and inserted the multiple resonant terms into the sliding surface

Manuscript received August 24, 2019; revised November 12, 2019, January 17, 2020, and March 13, 2020; accepted April 20, 2020. Date of publication April 26, 2020; date of current version July 31, 2020. This work was supported in part by the National Natural Science Foundation of China under Grants 51877130 and 51561165013, in part by the Shanghai Science and Technology Commission under Grant 17040501500, and in part by the National Key Research and Development Project of China under Grant 2017YFGH001164. Recommended for publication by Associate Editor T. Suntio. *(Corresponding author: Weimin Wu.)*

Han Li, Weimin Wu, and Min Huang are with the Department of Electrical Engineering, Shanghai Maritime University, Shanghai 201306, China (e-mail: 626142955@qq.com; wmwu@shmtu.edu.cn; minhuang@shmtu.edu.cn).

Henry Shu-hung Chung is with the Department of Electrical Engineering and the Centre for Smart Energy Conversion and Utilization Research, City University of Hong Kong, Hong Kong (e-mail: eeshc@cityu.edu.hk).

Marco Liserre is with the Chair of Power Electronics, Christian-Albrechts University of Kiel, 24118 Kiel, Germany (e-mail: ml@tf.uni-kiel.de).

Frede Blaabjerg is with the Department of Energy Engineering, Aalborg University, 9100 Aalborg, Denmark (e-mail: fbl@et.aau.dk).

This article has supplementary downloadable material available at https://ieeexplore.ieee.org, provided by the authors.

Color versions of one or more of the figures in this article are available online at https://ieeexplore.ieee.org.

Digital Object Identifier 10.1109/TPEL.2020.2990496

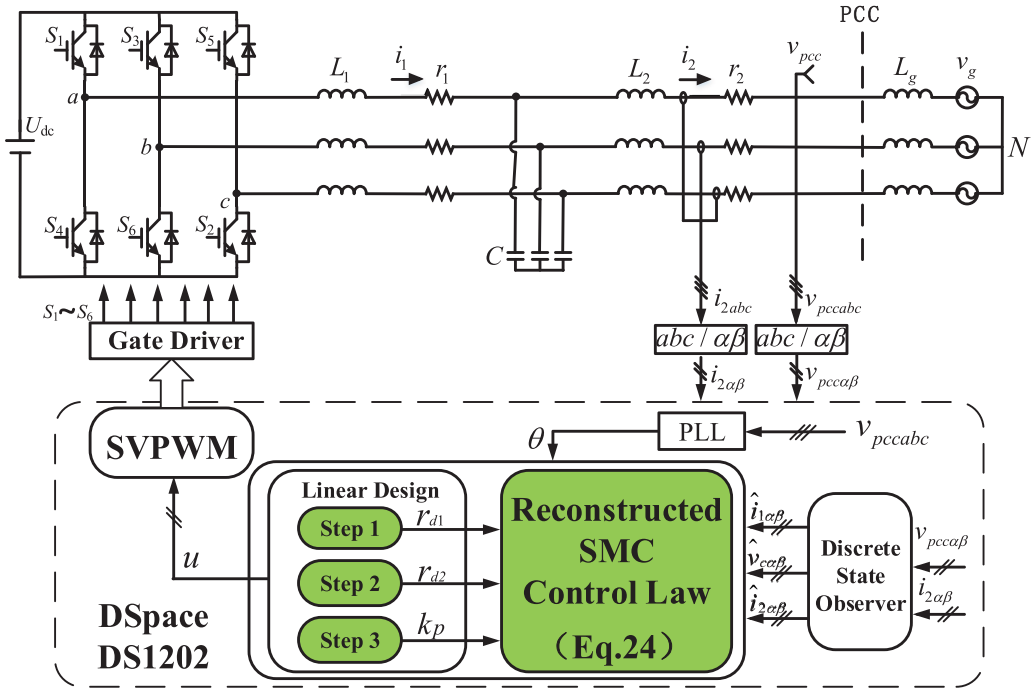

Fig. 1. Three-phase *LCL*-filtered GCI with the proposed design of the SMC controller using the linearized model.

function, which can eliminate the steady-state error and suppress the total harmonic distortion of the grid current effectively. Vieira *et al*. [30] introduced a dual-loop design strategy and chose the discrete-time SMC controller as the inner loop controller to simplify the current control design. Alali *et al*. [31] studied two continuous SMC algorithms to prevent very high-frequency switching effects of the SMC. Although all the mentioned PWM-SMC methods can achieve good control performance, the detailed design guideline of the controller parameters is lacking, resulting in the industrial application difficulty.

Aiming at the industrial application, different from the traditional PWM-SMC design based on Lyapunov stability, this article proposes a step-by-step design guideline of the PWM-SMC controller using a linearized model for the three-phase *LCL*-filtered GCIs, which can help engineers to precisely design a highly robust PWM-SMC controller to against the output filter parameters drift.

The rest of this article is organized as follows. Section II first presents the accurate error dynamics modeling of GCI with the *LCL* filter. Then, the essence of HM-SMC and PWM-SMC is explored in detail in Section III. Based on the above, Section IV proposes a novel design of the SMC controller using the linearized model together with a step-by-step parameter tuning and robustness analysis. Furthermore, Section V briefly introduces how to adopt a discrete state observer to save sensors, while Section VI demonstrates the experimental validation results on a 3 kW/3-phase/110 V experimental lab setup. Section VII discusses the comparison between the proposed control strategy with the existing SMC methods and the full-state feedback controller. Finally, Section VIII concludes the article.

II. Error Dynamics Modeling of GCI With the *LCL* Filter

Fig. 1 shows the three-phase *LCL*-filtered GCI and its basic control structure, where the *LCL* filter consists of an inverter-side inductor L_1, a capacitor C, and a grid-side inductor L_2. The equivalent grid impedance is modeled with the inductor L_g. The point of common coupling voltage $v_{\rm pcc} = [\,v_{\rm pcca}\ v_{\rm pccb}\ v_{\rm pccc}\,]^T$, the inverter-side current $i_1 = [\,i_{1a}\ i_{1b}\ i_{1c}\,]^T$, the capacitor voltage $v_c = [\,v_{ca}\ v_{cb}\ v_{cc}\,]^T$, and the grid-injected current $i_2 = [\,i_{2a}\ i_{2b}\ i_{2c}\,]^T$ are sensed or calculated for the controller.

The operation of the system in the α-β reference frame can be described as follows:

$$L_1\frac{di_{1\alpha}}{dt} = u_{i\alpha} - i_{1\alpha}r_1 - v_{c\alpha} \tag{1}$$

$$L_1\frac{di_{1\beta}}{dt} = u_{i\beta} - i_{1\beta}r_1 - v_{c\beta} \tag{2}$$

$$C\frac{dv_{c\alpha}}{dt} = i_{1\alpha} - i_{2\alpha} \tag{3}$$

$$C\frac{dv_{c\beta}}{dt} = i_{1\beta} - i_{2\beta} \tag{4}$$

$$L_2\frac{di_{2\alpha}}{dt} = v_{c\alpha} - i_{2\alpha}r_2 - v_{\rm pcc\alpha} \tag{5}$$

$$L_2\frac{di_{2\beta}}{dt} = v_{c\beta} - i_{2\beta}r_2 - v_{\rm pcc\beta} \tag{6}$$

where $u_{ik(k=\alpha,\beta)}$ is the switching function, and r_1 and r_2 are the equivalent resistances of inductors L_1 and L_2, respectively.

According to the angle generated by the phase-locked loop and the given reference current, the reference of grid-injected

current i_2^* can be obtained. Furthermore, based on (1)–(6), the reference of the inverter-side current i_1^* and the reference of capacitor voltage v_c^* can be also derived. Then the three references of the state variables are

$$\begin{cases} i_{2k}^* = I_2 \sin(\omega t + \theta) \\ v_{ck}^* = L_2 \dot{i}_{2k}^* + v_{\rm pcc} + i_{2k}^* r_2 \quad k = \alpha, \beta \\ i_{1k}^* = i_{2k}^* + C \dot{v}_{ck}^*. \end{cases} \tag{7}$$

Note that the α-axis and the β-axis are independent to each other. In order to facilitate the description, the next design focuses on the α-axis, while the design in the β-axis is the same as the one in the α-axis.

Defining the three system error dynamics as follows:

$$\begin{cases} x_{e1} = i_1^* - i_1 \\ x_{e2} = v_c^* - v_c \\ x_{e3} = i_2^* - i_2 \end{cases} \tag{8}$$

where their derivatives are

$$\begin{aligned} \dot{x_{e1}} &= \dot{i_1^*} - \dot{i_1} \\ &= \dot{i_1^*} - \left(\frac{1}{L_1} (u_i - i_1 r_1 + i_1^* r_1 - i_1^* r - v_c + v_c^* - v_c^*) \right) \\ &= -\frac{1}{L_1} x_{e2} - \frac{r_1}{L_1} x_{e1} - \frac{1}{L_1} u_i + \dot{i_1^*} + \frac{v_c^*}{L_1} + \frac{r_1}{L_1} i_1^* \end{aligned} \tag{9}$$

$$\dot{x_{e2}} = \dot{v_c^*} - \dot{v_c} = \frac{1}{C}(i_1^* - i_2^*) - \frac{1}{C}(i_1 - i_2) = \frac{1}{C} x_{e1} - \frac{1}{C} x_{e3} \tag{10}$$

$$\begin{aligned} \dot{x_{e3}} &= \dot{i_{e2}^*} - \dot{i_{e2}} = \frac{1}{L_2}(v_c^* - i_2^* r_2 - v_{\rm pcc}) \\ &\quad - \frac{1}{L_2}(v_c - i_2 r_2 - v_{\rm pcc}) = \frac{1}{L_2} x_{e2} - \frac{r_2}{L_2} x_{e3}. \end{aligned} \tag{11}$$

The state-space expression of the system error dynamics can be achieved as

$$\begin{aligned} \dot{x_e} &= A x_e + B u_i + D \\ \begin{bmatrix} \dot{x_{e1}} \\ \dot{x_{e2}} \\ \dot{x_{e3}} \end{bmatrix} &= \begin{bmatrix} -\frac{r_1}{L_1} & -\frac{1}{L_1} & 0 \\ \frac{1}{C} & 0 & -\frac{1}{C} \\ 0 & \frac{1}{L_2} & -\frac{r_2}{L_2} \end{bmatrix} \begin{bmatrix} x_{e1} \\ x_{e2} \\ x_{e3} \end{bmatrix} \\ &\quad + \begin{bmatrix} -\frac{1}{L_1} \\ 0 \\ 0 \end{bmatrix} \begin{bmatrix} u_i \\ 0 \\ 0 \end{bmatrix} + \begin{bmatrix} d_e \\ 0 \\ 0 \end{bmatrix} \end{aligned} \tag{12}$$

where $d_e = \dot{i_1^*} + \frac{v_c^*}{L_1} + \frac{r_1 i_1^*}{L_1}$.

III. Essence of HM-SMC and PWM-SMC

A. Basic Principle of the SMC Theory

For a given control system represented by the state equation

$$\dot{x} = A(x,t) + B(x,t)u \tag{13}$$

in order to construct an SMC system, the following two steps are needed [32]:

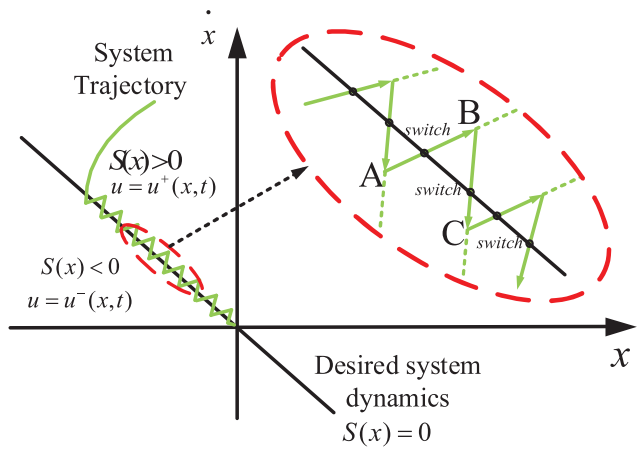

Fig. 2. Basic principle of the practical SMC system.

1) design a sliding surface $S(x) = 0$ to represent the desired system dynamics;
2) design a variable structure control $u(x,t)$ as

$$u(x,t) = \begin{cases} u^+(x,t) & \text{when} \quad S(x) > 0 \\ u^-(x,t) & \text{when} \quad S(x) < 0. \end{cases} \tag{14}$$

Any state x outside the sliding surface can be driven to reach the sliding surface in a finite time. On the sliding surface, the sliding mode takes place, following the desired system dynamics.

Fig. 2 introduces the basic principle of the practical SMC system. The middle black line represents the sliding surface $S(x) = 0$, which is the desired system dynamics. The sliding surface divides the system state into two different parts, where the different control of $u(x,t)$ works. Under this variable structure control, the green solid line depicts the system trajectory.

As shown in Fig. 2, when the system state is at point A, the sliding surface function $S(x)$ is less than zero and then $u^-(x,t)$ controls the system state to move toward the sliding surface. When the system state reaches the sliding surface, it crosses the sliding surface under the control of $u^-(x,t)$. At this time, the system switches to the control of $u^+(x,t)$ immediately. Due to the inertia (space or time lag), the system state can only gradually stop at point B. Then the system state moves from point B toward point C, according to the previous motion mode. The dashed line represents that the trajectory of the system state would be unstable without the switching control.

Through the above-mentioned analysis, we can find that switching plays an important role in the SMC system. For example, the reaching law approach is an effective way to design the SMC system [33], which directly specifies the dynamics of the sliding surface function

$$\dot{S} = -kS - \varepsilon \mathrm{sgn}(S). \tag{15}$$

The symbolic function could enable the system state to have a certain rate when reaching the sliding surface so that the system state can cross the sliding surface. Therefore, in a conventional SMC system, the switching of the system can be realized by the symbolic function in (15). However, in practical applications,

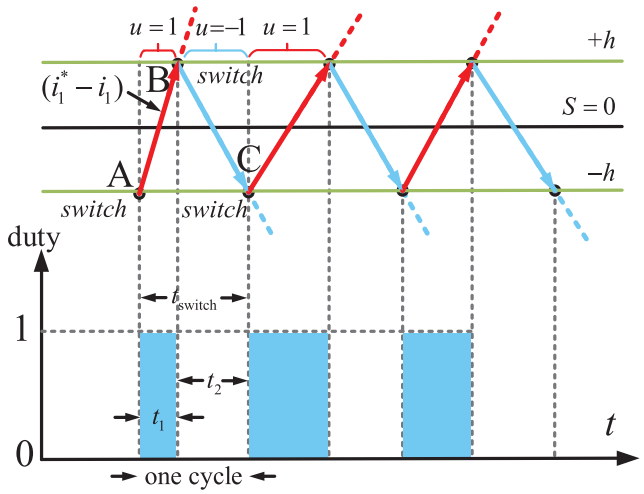

Fig. 3. Operation of HM-SMC.

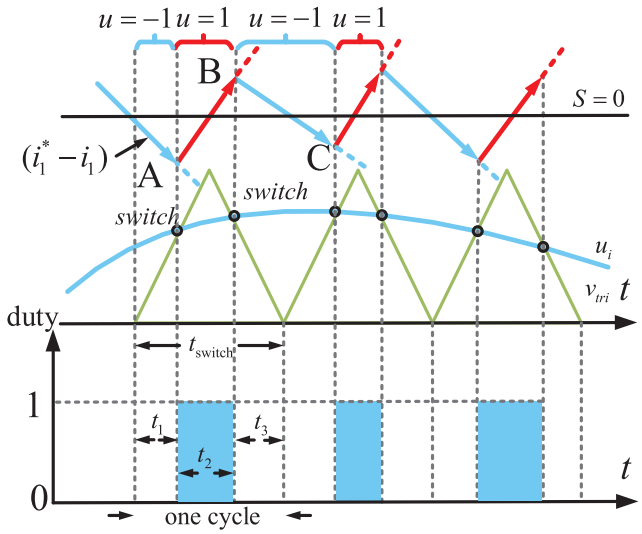

Fig. 4. Operation of PWM-SMC.

the switching modes are various, especially for the power-electronic-based systems with two special modulation modes. Here, a single-phase full-bridge GCI with an L filter is taken as an example to simply elaborate the switching characteristic in HM-SMC and PWM-SMC in the following two sections.

B. Switching Characteristic in HM-SMC

Fig. 3 shows the operation of HM-SMC, where this method adopts the hysteresis modulation to achieve a high-frequency switching action. For conveniently describing the system, the sliding surface function is chosen as the error of the inverter-side current of $(i_1^* - i_1)$.

The switching action can be written as

$$u = \begin{cases} -1 & S \geq +h \\ 1 & S \leq -h \end{cases} \tag{16}$$

where in the other case $(-h < S < +h)$, the switching action keeps the former state. h is the width of the hysteresis band, which controls the switching frequency.

As shown in Fig. 3, the hysteresis modulator employs a hysteresis band with the boundary layer to switch the control of the system. In one switching cycle, there are two periods t_1 and t_2, where the switching actions are $u = 1$ and $u = -1$, respectively.

When the sliding surface function $S(x)$ is equal to the value of the lower boundary layer $(-h)$ at point A, the switching occurs and the switching action is $u = 1$. During the switching action of $u = 1$, the sliding surface function $S(x)$ moves from $-h$ toward $+h$.

When the sliding surface function $S(x)$ is equal to the value of the upper boundary layer $(+h)$ at point B, the switching occurs and the switching action is $u = -1$. During the switching action of $u = -1$, the sliding surface function $S(x)$ moves from $+h$ toward $-h$.

Stated thus, the hysteresis modulator ensures the switching of the HM-SMC system.

C. Switching Characteristic in PWM-SMC

As shown in Fig. 4, different from the HM-SMC, the PWM-SMC adopts a pulsewidth modulator to control the system state to move toward the sliding surface indirectly. In one switching cycle, there are two circuit states, where the switching actions are $u = -1$ and $u = 1$, respectively.

When the system state is at point A, modulation wave u_i intersects the carrier, the switching occurs and the switching action is $u = 1$. During the switching action of $u = 1$, the sliding surface function $S(x)$ moves from the negative toward the positive.

When the system state is at point B, modulation wave u_i intersects the carrier again, the switching occurs and the switching action is $u = -1$. During the switching action of $u = -1$, the sliding surface function $S(x)$ moves from the positive toward the negative.

Similar to HM-SMC, the pulsewidth modulator can also ensure the switching of the PWM-SMC system. Although the conclusion is based on a single-phase GCI system, it can be extended to a three-phase GCI system.

Therefore, different from the conventional PWM-SMC design with the nonlinear term in u_i, the nonlinear term will be eliminated in the proposed design process, where the linear tool can be utilized to analyze the stability. Note that during the design, the PWM-SMC systems in [34]–[36] had also ignored the nonlinear term in the control law.

IV. Proposed Design of the PWM-SMC Controller Using the Linearized Model

A. Proposed Reconstructed Control Law With Zero Steady-State Error

The *LCL*-filtered GCI is a typical third-order system. In order to guarantee the global stability and damping effect, we choose the sum of three error dynamics as the sliding surface function,

which is defined as [29]

$$\begin{aligned} S &= C_e x_e \\ &= \alpha_1 x_{e1} + \alpha_2 x_{e2} + \alpha_3 x_{e3} \\ &= \alpha_1 (i_1^* - i_1) + \alpha_2 (v_c^* - v_c) + \alpha_3 (i_2^* - i_2). \end{aligned} \tag{17}$$

Through the above-mentioned analysis, the switching function can be realized by pulsewidth modulation (PWM). Thus, the symbolic function is eliminated and the reaching law is rewritten as

$$\dot{S} = -kS. \tag{18}$$

Based on (17) and (18), a control law is deduced as follows:

$$\begin{aligned} u_i = &-r_1 x_{e1} - x_{e2} + L_1 \dot{i}_1^* + v_c^* + r_1 i_1^* + L_1 \frac{\alpha_2}{\alpha_1} \left(\frac{1}{C} x_{e1} - \frac{1}{C} x_{e3} \right) \\ &+ L_1 \frac{\alpha_3}{\alpha_1} \left(\frac{1}{L_2} x_{e2} - \frac{r_2}{L_2} x_{e3} \right) + k \frac{L_1}{\alpha_1} S. \end{aligned} \tag{19}$$

Through (19), we find that the control law is complex, resulting in the difficulty to design controller parameters.

Separating the sliding surface function, the control law can be rewritten as

$$\begin{aligned} u_i = &L_1 \dot{i}_1^* + v_c^* + r_1 i_1^* + \left(-r_1 + L_1 \frac{\alpha_2}{\alpha_1} \frac{1}{C} + k L_1 \right) x_{e1} \\ &+ \left(-1 + L_1 \frac{\alpha_3}{\alpha_1} \frac{1}{L_2} + k \frac{L_1}{\alpha_1} \alpha_2 \right) x_{e2} \\ &+ \left(-L_1 \frac{\alpha_2}{\alpha_1} \frac{1}{C} - L_1 \frac{\alpha_3}{\alpha_1} \frac{r_2}{L_2} + k \frac{L_1}{\alpha_1} \alpha_3 \right) x_{e3}. \end{aligned} \tag{20}$$

As shown in (20), the gain of each state feedback variable is determined by three or four sliding-mode parameters (sliding surface function parameters and the gain of the reaching law). Based on (20), by simplifying the control law and reintegrating the sliding-mode parameters, three new uncoupled controller parameters can be obtained. They are as follows:

$$r_{d1} = \left(-r_1 + L_1 \frac{\alpha_2}{\alpha_1} \frac{1}{C} + k L_1 \right) \tag{21}$$

$$r_{d2} = \left(-1 + L_1 \frac{\alpha_3}{\alpha_1} \frac{1}{L_2} + k \frac{L_1}{\alpha_1} \alpha_2 \right) \tag{22}$$

$$r_{d3} = \left(-L_1 \frac{\alpha_2}{\alpha_1} \frac{1}{C} - L_1 \frac{\alpha_3}{\alpha_1} \frac{r_2}{L_2} + k \frac{L_1}{\alpha_1} \alpha_3 \right). \tag{23}$$

Note that, using the determined new three controller parameters to solve the original sliding surface function parameters and the gain of the reaching law, we can obtain an infinite number of solutions. Thus, the sliding surface function parameters and the gain of the reaching law must exist. As long as the sliding surface passes through the origin, the system would converge to the origin, where the Lyapunov stability of PWM-SMC is not affected.

Therefore, a new control law can be derived as

$$u_i = L_1 d_e + r_{d1} x_{e1} + r_{d2} x_{e2} + r_{d3} x_{e3}. \tag{24}$$

However, in a practical system, the *LCL* filter parameters and parasitic resistances have tolerances. L_1, L_2, C, r_1, and r_2 represent the actual parameters of the system, while L'_1, L'_2, C', r'_1, and r'_2 represent the estimated parameters, respectively. There is a deviation between the actual parameter and the estimated one, and the *LCL* filter parameters used in the PWM-SMC controller are the estimated parameter. According to [29], this deviation would cause the steady-state error of the system, where the multiple resonant terms can effectively eliminate it. Therefore, in our case, a proportional resonant (PR) term is used instead of the gain of r_{d3}, and the transfer function is

$$G_c(s) = k_p + \frac{2 k_r \omega_i s}{s^2 + 2\omega_i s + {\omega_0}^2} \tag{25}$$

where k_p and k_r are the proportional and resonant gains, and $\omega_i$andω_o are the cutoff frequency and the fundamental frequency, respectively.

Due to the adoption of digital control, it is necessary to consider the delay issue after obtaining the control law. T_s is the sampling period. The zero-order hold is

$$G_{\mathrm{zoh}}(s) = \frac{1 - e^{-T_s \cdot s}}{s}. \tag{26}$$

Thus, when a T_s computation delay is addressed, the total delay $G_d(s)$ is

$$G_d(s) = \frac{1}{T_s} e^{-T_s \cdot s} G_{\mathrm{zoh}}(s) \approx e^{-1.5 T_s \cdot s}. \tag{27}$$

Thus, the whole control block diagram of the proposed design of the SMC controller using the linearized model can be drawn in Fig. 5.

The closed-loop transfer function is

$$G(s) = \frac{I_2(s)}{I_2^*(s)} = \frac{a_5 s^5 + a_4 s^4 + a_3 s^3 + a_2 s^2 + a_1 s + a_0}{b_5 s^5 + b_4 s^4 + b_3 s^3 + b_2 s^2 + b_1 s + b_0} \tag{28}$$

where

$$\begin{aligned} a_5 &= C'_f L'_1 L'_2 \\ a_4 &= C'_f L'_1 r'_2 + C'_f L'_2 r'_1 + C'_f L'_2 r_{d1} + 2 C'_f L'_1 L'_2 \omega_i \\ a_3 &= C'_f L'_1 L'_2 \omega_o^2 + L'_1 + L'_2 + L'_2 r_{d2} + C'_f r'_1 r'_2 \\ &\quad + C'_f r'_2 r_{d1} + 2 C'_f L'_1 r'_2 \omega_i + 2 C'_f L'_2 r'_1 \omega_i + 2 C'_f L'_2 r_{d1} \omega_i \\ a_2 &= k_p + r'_1 + r'_2 + r_{d1} + 2 L'_1 \omega_i + 2 L'_2 \omega_i + r'_2 r_{d2} \\ &\quad + 2 L'_2 r_{d2} \omega_i + C'_f L'_1 r'_2 \omega_o^2 + C'_f L'_2 r'_1 \omega_o^2 + C'_f L'_2 r_{d1} \omega_o^2 \\ &\quad + 2 C'_f r'_1 r'_2 \omega_i + 2 C'_f r'_2 r_{d1} \omega_i \\ a_1 &= 2 k_p \omega_i + 2 k_r \omega_i + 2 r'_1 \omega_i + 2 r'_2 \omega_i \\ &\quad + 2 r_{d1} \omega_i + L'_1 \omega_o^2 + L'_2 \omega_o^2 + 2 L'_1 \omega_i + 2 L'_2 \omega_i \\ &\quad + 2 r'_2 r_{d2} \omega_i + L'_2 r_{d2} \omega_o^2 + C'_f r'_1 r'_2 \omega_o^2 + C'_f r'_2 r_{d1} \omega_o^2 \\ a_0 &= k_p \omega_o^2 + r'_1 \omega_o^2 + r'_2 \omega_o^2 + r_{d1} \omega_o^2 + r'_2 r_{d2} \omega_o^2 \\ b_5 &= C_f L_1 L_2 e^{1.5 s \cdot T_s} \\ b_4 &= C_f L_2 r_{d1} + C_f L_1 r_2 e^{1.5 s \cdot T_s} + C_f L_2 r_1 e^{1.5 s \cdot T_s} \\ &\quad + 2 C_f L_1 L_2 \omega_i e^{1.5 s \cdot T_s} \\ b_3 &= C_f L_1 L_2 e^{1.5 s \cdot T_s} \omega_o^2 + L_2 r_{d2} + L_1 e^{1.5 s \cdot T_s} \end{aligned}$$

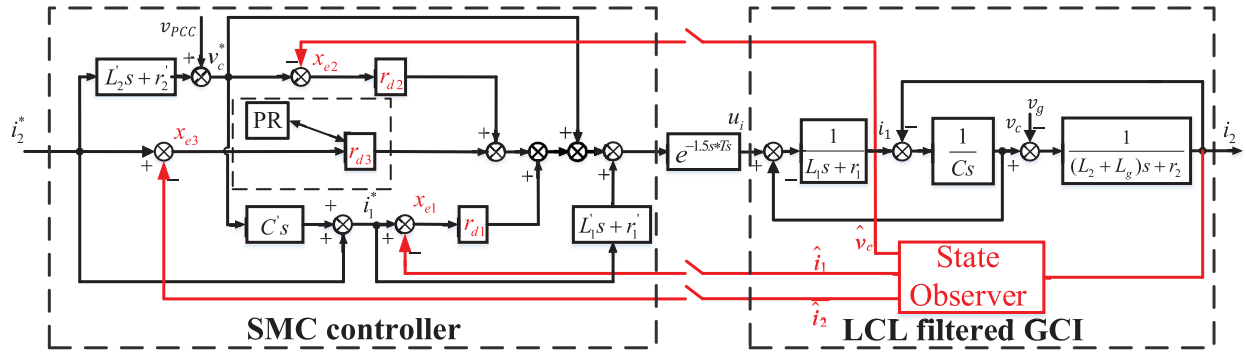

Fig. 5. Block diagram of the proposed design of the SMC controller using the linearized model.

$$+ L_2e^{1.5s\cdot T_s} + C_fr_2r_{d1} + C_fr_1r_2e^{1.5s\cdot T_s} + 2C_fL_2r_{d1}\omega_i$$
$$+ 2C_fL_1r_2\omega_ie^{1.5s\cdot T_s} + 2C_fL_2r_1\omega_ie^{1.5s\cdot T_s}$$

$$b_2 = k_p + r_{d1} + r_2r_{d2} + r_1e^{1.5s\cdot T_s} + r_2e^{1.5s\cdot T_s} + 2L_2r_{d2}\omega_i$$
$$+ 2L_1\omega_ie^{1.5s\cdot T_s} + 2L_2\omega_ie^{1.5s\cdot T_s} + C_fL_2r_{d1}\omega_o^2$$
$$+ 2C_fr_2r_{d1}\omega_i + 2C_fr_1r_2\omega_ie^{1.5s\cdot T_s} + C_fL_1r_2\omega_o^2e^{1.5s\cdot T_s}$$
$$+ C_fL_2r_1\omega_o^2e^{1.5s\cdot T_s}$$

$$b_1 = 2k_p\omega_i + 2k_r\omega_i + 2r_{d1}\omega_i + L_1\omega_o^2e^{1.5s\cdot T_s}$$
$$+ L_2\omega_o^2e^{1.5s\cdot T_s} + 2r_2r_{d2}\omega_i + 2r_1\omega_ie^{1.5s\cdot T_s} + 2r_2\omega_ie^{1.5s\cdot T_s}$$
$$+ L_2r_{d2}\omega_o^2 + C_fr_2r_{d1}\omega_o^2 + C_fr_1r_2\omega_o^2e^{1.5s\cdot T_s}$$

$$b_0 = k_p\omega_o^2 + r_1\omega_o^2e^{1.5s\cdot T_s} + r_2\omega_o^2e^{1.5s\cdot T_s} + r_{d1}\omega_o^2 + r_2r_{d2}\omega_o^2.$$

As shown in Fig. 5, although compared with the conventional SMC control law, the reconstructed SMC control law has been simplified, there are still three cascaded control loops and three feedforward terms in our control diagram. It is still a big challenge for engineers to design the controller.

Here, a three-loop step-by-step design procedure will be introduced. The design flowchart is shown in Fig. 6. First, based on the nominal *LCL* filter parameters ($L_1 = 1.2$ mH, $L_2 = 1.2$ mH, and $C = 6$ μF), the inner inverter-side current loop is designed and the controller parameter r_{d1} is selected. Second, based on the previous controller parameter r_{d1}, the middle loop of the capacitor voltage feedback is designed and the controller parameter r_{d2} is chosen. Third, the outer PR controller is designed, according to the previous controller parameters r_{d1} and r_{d2}. Finally, the verification of robustness against the *LCL* filter parameters drift is addressed, after selecting the controller parameters.

It is worth mentioning that the following method can get the approximate stability regions of the inner and middle loop. The outer loop would ultimately determine the stability of the system. Due to the complexity of the control diagram, through this design procedure, only a set of better parameters can be obtained, but the optimal controller parameters are hardly chosen. During the stability analysis, the sample frequency is set as 12 kHz, which is equal to the switching frequency.

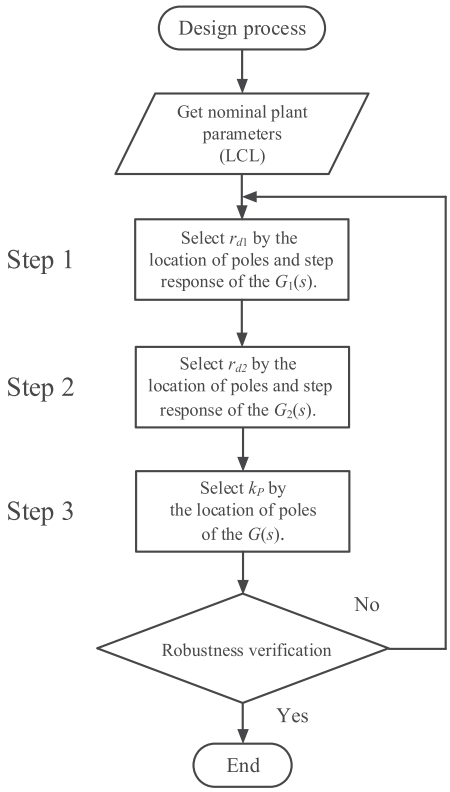

Fig. 6. Proposed design flowchart.

B. Step-By-Step Parameters Tuning

Step 1—Design the Gain r_{d1}: The control block diagram of the inverter-side current loop is shown in Fig. 7. Here, the reference and the feedback of the capacitor voltage are both regarded as perturbation terms. The closed-loop transfer function is

$$G_1(s) = \frac{i_1(s)}{i_1^*(s)} = \frac{L_1's + r_1' + r_{d1}}{(L_1e^{1.5s*T_s})s + r_{d1} + r_1e^{1.5s\cdot T_s}}. \quad (29)$$

In order to facilitate the observation of the location of the poles and improve the accuracy of the digital realization, the transfer function in the above-mentioned continuous domain is linearly discretized by MATLAB. Fig. 8 shows the discrete closed-loop

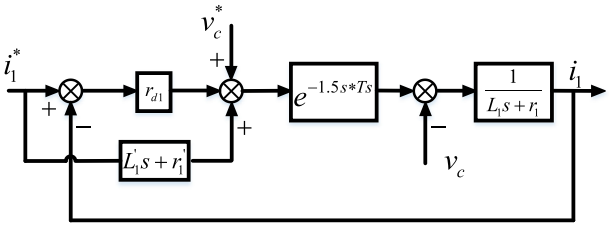

Fig. 7. Block diagram of the inverter-side current loop.

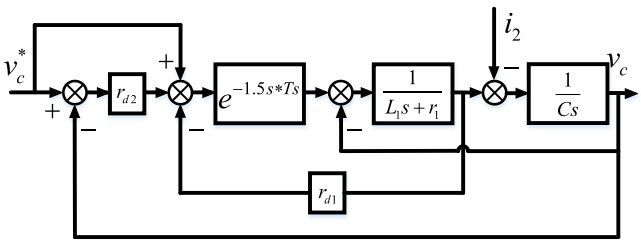

Fig. 10. Block diagram of the capacitor voltage loop.

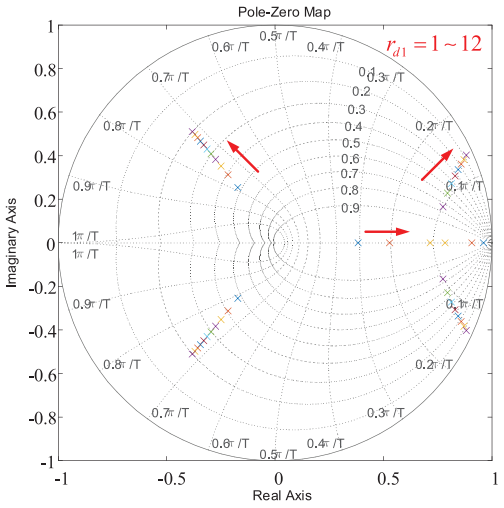

Fig. 8. Closed-loop pole locations of G_1(s), when r_{d1} varies from 1 to 12.

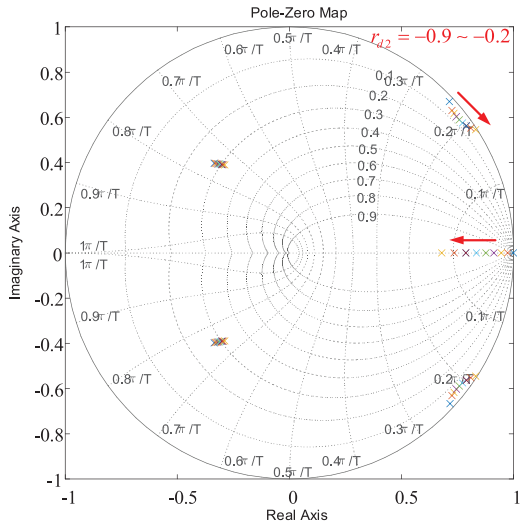

Fig. 11. Closed-loop pole locations of $G_2(s)$, when r_{d2} varies from -0.9 to -0.2.

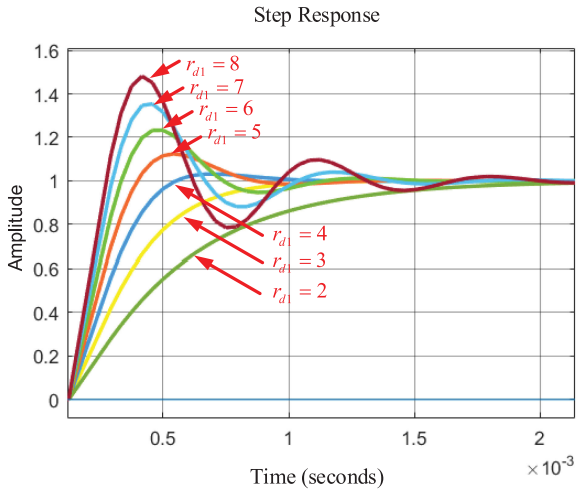

Fig. 9. Step responses of $G_1(s)$ with different r_{d1}.

pole locations of (29). It can be seen that the poles are located inside the unit circle, as long as the gain r_{d1} is less than 12.

In order to assist with selecting the value of r_{d1}, the step responses of $G_1(s)$ with different r_{d1} are illustrated in Fig. 9, where the preferred region of r_{d1} range is between 3 and 6. Here, r_{d1} is chosen as 4.

Step 2—Design the Gain r_{d2}: The design of r_{d2} is similar to that of r_{d1}. The diagram of the middle loop of the capacitor voltage feedback is depicted in Fig. 10, where the inverter-side current reference and the grid-injected current feedback are regarded as disturbance terms. The closed-loop transfer function is

$$G_2(s)=\frac{v_c(s)}{v_c^*(s)}=\frac{1+r_{d2}}{(CL_1e^{1.5s\cdot T_s})s^2+(Cr_{d1}+Cr_1e^{1.5s\cdot T_s})s+r_{d2}+e^{1.5s\cdot T_s}}. \tag{30}$$

Fig. 11 shows the closed-loop pole locations of $G_2(s)$, showing that the stable region of r_{d2} ranges from -0.9 to -0.2. This is an approximate range of the stability region, mainly to avoid introducing unstable poles.

Similarly, the step responses of $G_2(s)$ with different r_{d2} are illustrated in Fig. 12. Here, r_{d2} is chosen as -0.4.

Step 3—Design the Proportional Gain k_P: Although the PR controller is adopted, the stability of the system mainly depends on the proportional term of k_P, since the resonant frequency is 50 Hz and the desired control bandwidth is far higher than 50 Hz. Therefore, the PR controller is simplified as k_P.

With r_{d1} and r_{d2}, the closed-loop pole locations of $G(s)$ are shown in Fig. 13, where it can be clearly seen that the stable region of k_P is between 1 to 12 and the critical value of k_P is about 13. Finally, k_P is selected as 10 to ensure sufficient control bandwidth and stable margin. The resonant term of k_r is just selected as an initial value. In our case, k_r is chose as 800.

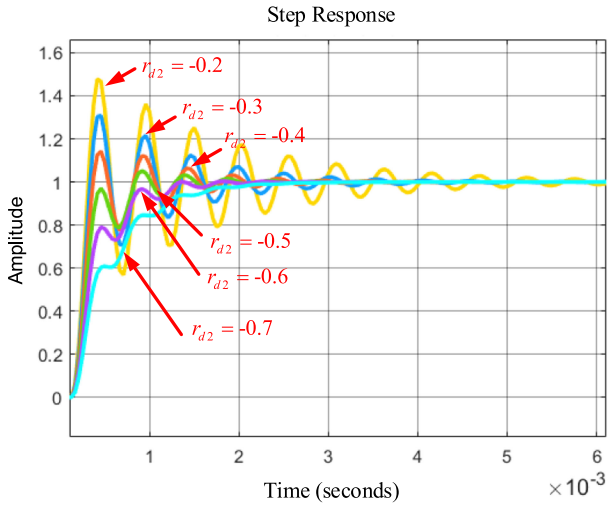

Fig. 12. Step responses of $G_2(s)$ with different r_{d2}.

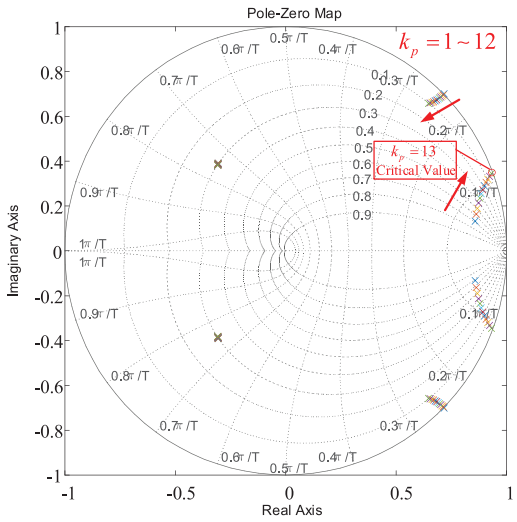

Fig. 13. Closed-loop pole locations of $G(s)$, when k_P varies from 1 to 12.

In particular, according to the actual situation, the harmonic compensators could be inserted into the PR controller to resist the low-order current harmonics caused by background harmonic voltages.

C. Robustness Analysis Against the Parameters Drift

Let the parameters of the *LCL* filter vary in a wide range. L_1 varies in the range of 0.8–2.0 mH (-33%–$+66\%$ of L_1), C varies in the range of 4–9 μF (-33%–$+50\%$ of C), and the grid-side inductance L_g varies in the range of 0–6 mH (0%–$+500\%$ of L_2), respectively. Then, the locations of the closed-loop poles of the system are derived. If the closed-loop poles of $G(s)$ are still located inside the unit circle, the system is stable, which means that the controller parameter is reasonable and feasible. If any closed-loop pole locations of the system are located outside the unit circle, the system is unstable. Then, we have to go back to redesign the gains of r_{d1}, r_{d2}, and k_p, and then test the robustness again. From Fig. 14, it can be clearly seen that all the closed-loop

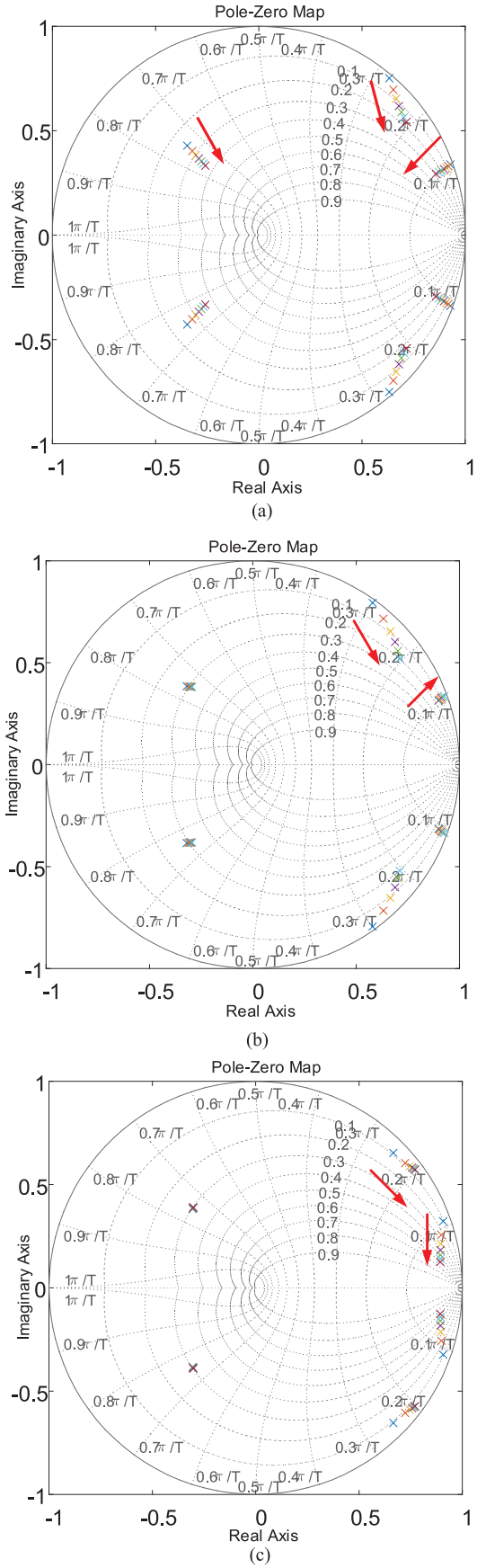

Fig. 14. Closed-loop pole locations of $G(s)$ when the filter parameter varies. (a) L_1 varies in the range of 0.8–2.0 mH. (b) C varies in the range of 4–9 μF. (c) L_g varies in the range of 0–6 mH.

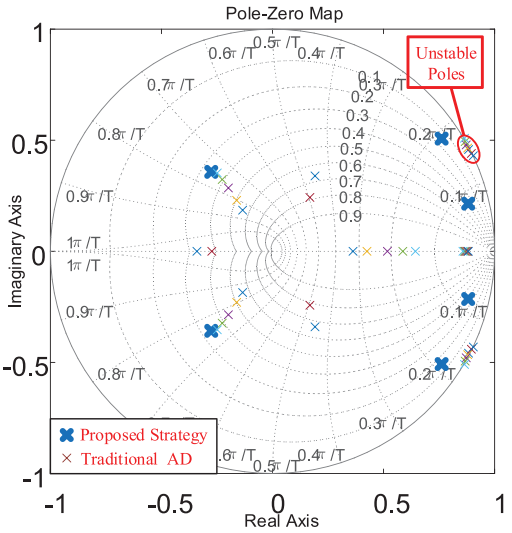

Fig. 15. Closed-loop pole locations of $G(s)$ with the traditional AD method and the proposed control strategy when the resonance frequency is about 2000 Hz ($f_s/6$).

poles of $G(s)$ are still located inside the unit circle when the parameters of the *LCL* filter vary in a wide range.

In order to furthermore evaluate the robustness of the proposed control strategy, a comparison between the traditional capacitor-current-feedback active damping (AD) method and the proposed method is performed. Notably, if the resonance frequency is equal to one-sixth of the sampling frequency and the total delay time is equal to one and a half sampling periods, the system can hardly be stable, no matter how much the capacitor-current-feedback coefficient is [37]. Here, the *LCL* parameters are set as $L_1 = 1.6$ mH, $L_2 = 1.2$ mH, $L_g = 1.9$ mH, and $C = 6$ μF, where the resonance frequency is about 2000 Hz $(f_s/6)$. As shown in Fig. 15, some closed-loop poles of G(s) with the traditional AD method are always located on the unit circle or outside the unit circle with various capacitor-current-feedback coefficients, while the closed-loop poles of G(s) with the proposed control strategy are all located inside the unit circle. It can be clearly proven that the proposed control strategy has a better stable region than the traditional capacitor-current-feedback AD method.

V. Brief Design of the Discrete State Observer

In order to save the total sensors, a simple and easily implemented discrete state observer is also adopted.

Based on (1)–(6), the discrete model of the system is obtained as

$$x(k+1) = A_d x(k) + B_d u_i(k) + D_d v_g(k) \tag{31}$$

$$A_d = \begin{bmatrix} 1 - \frac{r_1 T_s}{L_1} & -\frac{T_s}{L_1} & 0 \\ \frac{T_s}{C_f} & 1 & -\frac{T_s}{C_f} \\ 0 & \frac{T_s}{L_2} & 1 - \frac{r_2 T_s}{L_2} \end{bmatrix} \quad B_d = \begin{bmatrix} \frac{T_s V_{\rm dc}}{L_1} \\ 0 \\ 0 \end{bmatrix}$$

$$C_d = \begin{bmatrix} 0 \\ 0 \\ 1 \end{bmatrix} \quad D_d = \begin{bmatrix} 0 \\ 0 \\ \frac{T_s v_{\rm pcc}}{L_2} \end{bmatrix}.$$

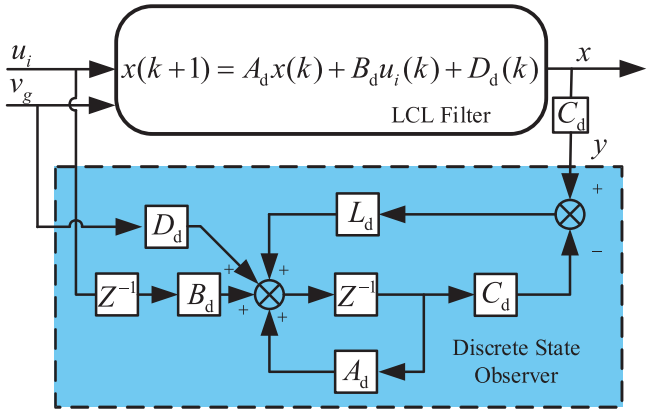

Fig. 16. Structure of the discrete state observer.

As shown in Fig. 16, the discrete state observer is given by

$$\begin{cases} \widehat{x}(k+1) = A_d \widehat{x}(k) + B_d u_i(k) + D_d(k) + L_d\left[\widehat{y}(k) - y(k)\right] \\ \widehat{y}(k) = C_d \widehat{x}(k) \end{cases} \tag{32}$$

where the subscript "^" denotes the estimated value and L_d is the observer gain vector.

The design of L_d is carried out via the zero pole assignment. The poles of the closed-loop system consist of the union of the controller poles and the observer poles. A rule of thumb is to select the observer poles to be two to six times faster than the poles of the controller. Then, the observer dynamics do not limit the bandwidth determined by the controller.

Generally, if the poles of the observer are chosen as three to five times faster than those of the controller, the dynamic characteristics of the observer will not impose any restrictions on the bandwidth determined by the controller. However, the observers' poles should not exceed the Nyquist frequency.

The characteristic polynomial of the observer dynamics is selected as

$$\det(zI_3 - G + L_d C_d) = (z - p_1)(z - p_2)(z - p_3) \tag{33}$$

where p_1, p_2, and p_3 are the desired poles of the observer, then the observer gain vector can be calculated.

According to the principle of separation, the design of the state observer and current controller does not affect each other, which means the SMC and the state observer can be designed independently.

VI. Experimental Verifications

In order to validate the effectiveness of the proposed strategy, a prototype of 3-kW three-phase three-wire *LCL*-filter-based system with the proposed control scheme has been implemented by using the dSPACE DS1202. When constructing the control loop, the control law is discretized due to digital implementation. The power grid is emulated with Chroma 61830. The Yokogawa DL 1640 digital oscilloscope is used to measure the grid voltage waveform and grid-injected current waveform. The experimental setup is shown in Fig. 17, while the system parameters and nominal controller parameters are listed in Table I.

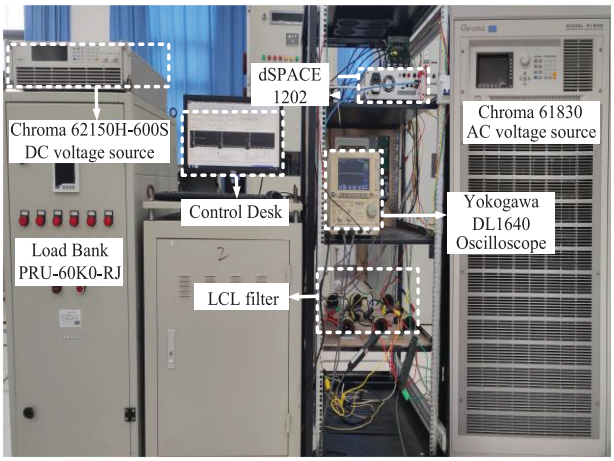

Fig. 17. Experimental setup.

TABLE I
SYSTEM PARAMETERS

Symbol	Value	Symbol	Value
Grid voltage v_g	110 V(RMS)	Switching frequency f_{sw}	12 kHz
DC link voltage U_{dc}	350 V	Sampling frequency f_s	12 kHz
Inverter-side inductor L_1	1.2 mH	Coefficient of control k_p	10
Grid-side inductor L_2	1.2 mH	Coefficient of control k_r	800
Filter capacitor C	6 μF	Coefficient of control k_{d1}	4
Equivalent series resistance of L_1	0.2Ω	Coefficient of control k_{d2}	-0.4
Equivalent series resistance of L_2	0.2Ω		

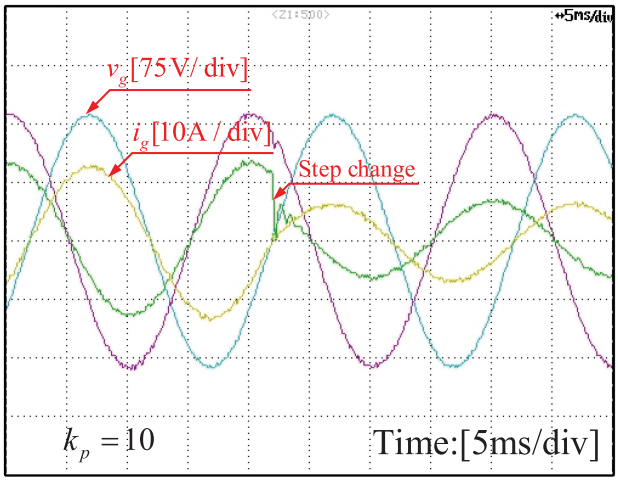

Fig. 18. Measured grid voltage waveform and grid-injected current waveform when $k_p = 10$.

A. *Performance Under Nominal* LCL *Parameters Condition*

Figs. 18 and 19 show the results under the nominal *LCL* parameters condition.

Fig. 18 shows that the grid-injected current can keep tracking the reference with the zero steady-state error when $k_p = 10$. In addition, the grid-injected current steps down from 12.86 to 6.43 A, where the proposed strategy exhibits a fast dynamic response, meaning that the system has achieved a wide control bandwidth.

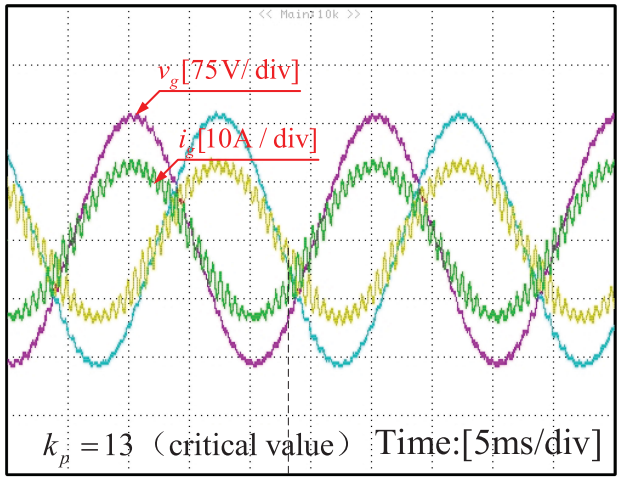

Fig. 19. Measured grid voltage waveform and grid-injected current waveform when $k_p = 13$.

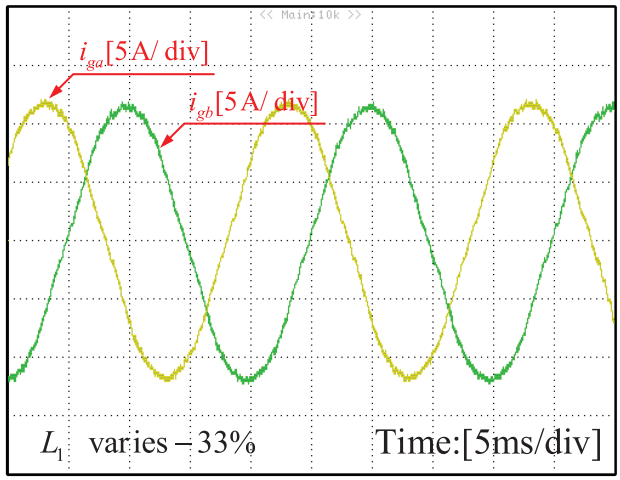

Fig. 20. Measured grid-injected current waveform when $L_1 = 0.8$ mH, $L_2 + L_g = 1.2$ mH, and $C = 6$ μF.

Fig. 19 shows that the measured grid voltage and grid-injected current oscillated when the gain k_p increased to 13 (critical value obtained by theory analysis), which matches the theoretical analysis in Fig. 13 quite well.

B. *Performance under* LCL *Filter Parameters Drift Condition*

To evaluate the robustness of the proposed control strategy, Figs. 20 and 21 show the grid-injected current under the condition of the *LCL* filter parameters drift (L_1 varies −33%, C varies −33% from the nominal values, respectively.). Despite the variations of the *LCL* filter parameters, the system can still be stable and achieve the zero steady-state error, which is a good agreement with the closed-loop pole locations of G(s) in Fig. 14.

In actual applications, the grid inductance may change in a large range, especially when multiple GCIs are in the parallel connection with the power grid at the same common coupling point [9]. To emulate this situation, the external inductors ($L_g = 6$ mH) are adopted. As shown in Fig. 22, the system remains

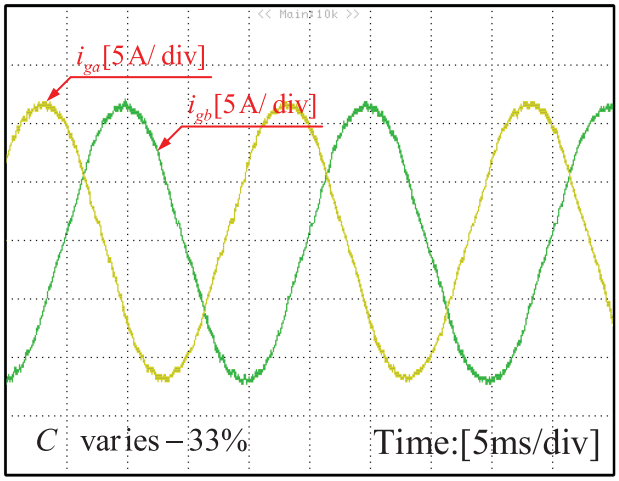

Fig. 21. Measured grid-injected current waveform when $L_1 = 1.2$ mH, $L_2 + L_g = 1.2$ mH, and $C = 4$ μF.

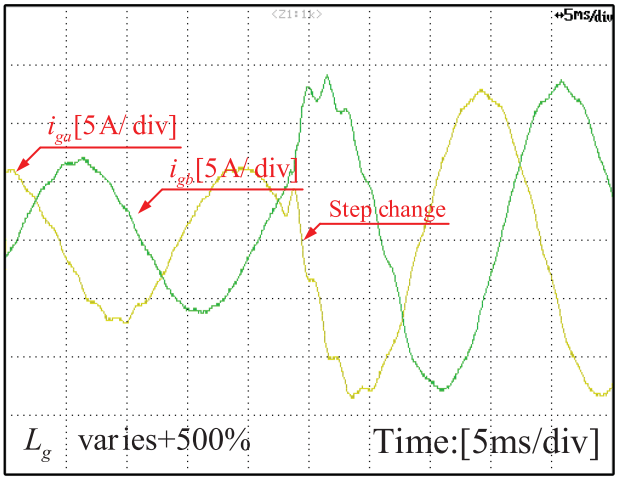

Fig. 22. Dynamic performance when $L_1 = 1.2$ mH, $L_2 + L_g = 7.2$ mH, and $C = 6$ μF.

stable with the zero steady-state error. It is worth mentioning that the large equivalent grid impedance usually leads to the decrease of the system control bandwidth. However, the transient response with the proposed control strategy is good (the settling time is within one cycle, as shown in Fig. 22), proving that the proposed strategy can also achieve a good control bandwidth.

Fig. 23 shows the grid-injected current with the capacitor-current-feedback AD method when the resonance frequency is about 2000 Hz (f_s/6). The system is unstable, which is consistent with the conclusions in [37]. Fig. 24 shows the grid-injected current with the proposed control strategy under the same condition, where the system is stable. It can be proven that the proposed control strategy has a wider stable region than that with the conventional capacitor-current-feedback AD method.

C. Performance Under a Distorted Grid

Fig. 25 shows the measured grid-injected current and grid voltage under a distorted grid. A programmable AC source

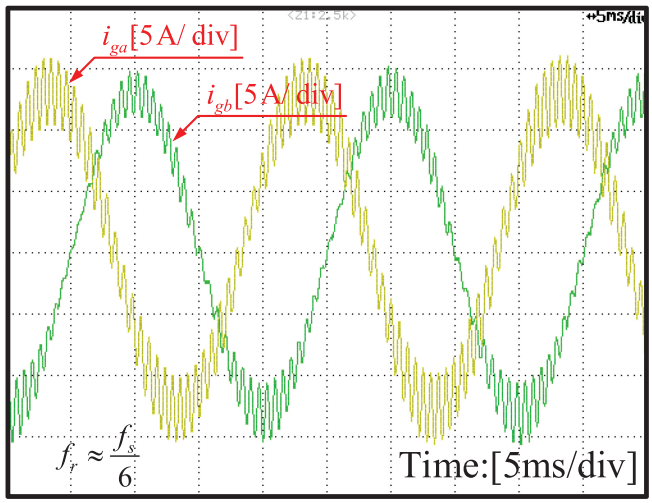

Fig. 23. Measured grid-injected current waveform with the capacitor-current-feedback AD when the resonance frequency is about 2000 Hz (f_s/6).

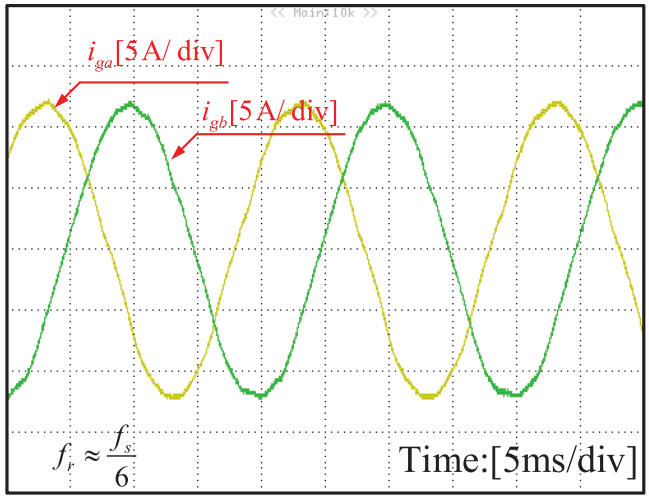

Fig. 24. Measured grid-injected current waveform with the proposed control strategy when the resonance frequency is about 2000 Hz (f_s/6).

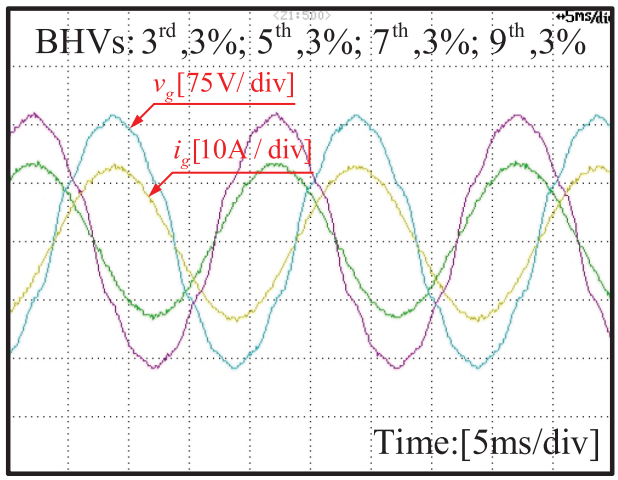

Fig. 25. Measured grid voltage waveform and grid-injected current waveform under a distorted grid.

TABLE II
COMPARISONS BETWEEN THE EXISTING SMC METHODS AND THE PROPOSED ONE

		HM-SMC			PWM-SMC		
Comparison category		[26]	[27]	[28]	[29]	[30]	Proposed
Sampling frequency		125 kHz	60 kHz	40 kHz	15 kHz	12 kHz	12 kHz
Switching frequency		18.8 kHz	6 kHz	6 kHz	15 kHz	12 kHz	12 kHz
Measured variables		3	2	2	4	4	2
Power Rating		3.3 kW	1.5 kW	1.5 kW	5 kW	3.2 kW	3 kW
LCL filter	L_1	1.74 mH	5 mH	7 mH	1.2 mH	1 mH	1.2 mH
	C	50 μF	6.8μF	6.8μF	50 μF	62 μF	6 μF
	L_2	0.6867 mH	2 mH	5 mH	0.4 mH	0.3 mH	1.2 mH
Harmonic rejection		Not reported	Good	Good	Good	Not reported	Good

(Chroma 61830) is utilized to emulate the grid voltage, which is distorted by the third, fifth, seventh, and ninth harmonics. The magnitudes of the harmonics with respect to the grid fundamental voltage are 3%, 3%, 3%, and 3%, respectively. Due to the PR term and the wide bandwidth of the system, the grid-injected current remains sinusoidal, which proves the proposed system has the strong ability to resist the adverse effect caused by the harmonic grid voltage.

VII. DISCUSSION

A. Comparison With the Existing SMC Methods

Through the experimental results, it can be observed that the proposed design guideline of the robust PWM-SMC controller is practical. A summary of the comparison between the existing SMC methods and the proposed SMC strategy is illustrated in Table II. The performance of the system is analyzed from the following perspectives: sampling frequency, switching frequency, number of measured state variables, power rating, *LCL* filter parameters, and harmonic rejection.

1) Hysteresis Modulation Based SMC: In [26]–[28], the hysteresis modulator is utilized to ensure the switching of the HM-SMC system. The width of the hysteresis band controls the switching frequency. Among these three cases, there are two obvious advantages: fast dynamic response (which means a high control bandwidth) and highly strong robustness. This is mainly because the hysteresis modulator directly realizes the switching of the system, which reflects the invariance of the SMC theory. However, the issue of the variable switching frequency introduced by the hysteretic modulator will impose a burden on the design of the *LCL* filter. For example, in [27] and [28], the total inductance is 7 mH and 12 mH, respectively, which may cost much. In addition, in order to achieve a good control effect, a high sampling frequency is needed. For example, the sampling frequency is 125 kHz in [26], which needs high requirements for digital control.

Compared with the above HM-SMC methods, the proposed control strategy adopts the PWM, where the switching frequency is fixed and the sampling frequency is low. Thus, the total inductance is 2.4 mH and the sampling frequency is 12 kHz. Although the dynamic response is not so fast as the one with HM-SMC, the experimental results show that the transient performance is acceptable.

2) Pulsewidth Modulation Based SMC: In [29] and [30], the PWM-SMC is used for the controller design, where the Lyapunov stability theorem is utilized to verify the stability of the system. However, this theorem cannot obtain an accurate stability region. Thus, in [29] and [30], the design of the SMC controller parameters had not been presented in detail.

Compared with the above PWM-SMC methods, the proposed control strategy analyzes the essence of the SMC and then provides an accurate and detailed design guideline, which can help engineers to precisely design a highly robust PWM-SMC controller.

In addition, the performance of the proposed PWM-SMC strategy is satisfactory, including the robustness, harmonic rejection, and steady-state error. Owing to the implementation of the discrete state observer, only two state variables are measured.

B. Comparison With the Full-State Feedback Controller

It is worth mentioning that the proposed PWM-SMC strategy utilized three state variables, which is in the same way as the full-state feedback controller. Indeed, from the perspective of the digital implementation, there is a little similarity between the two control methods.

However, from the perspective of the physical significance, the two control methods are totally different. The SMC strategy provides a nonlinear view on the control of the power electronics, where the physical significance, for example as shown in Figs. 2 and 4, is much more clear.

Furthermore, in the proposed PWM-SMC control law, there are some feedforward terms, which can have some effects on improving the dynamic response and eliminating the steady-state error. However, since the lack of the global system modeling, the full-state feedback controller does not have these feedforward terms.

VIII. CONCLUSION

This article presents a novel step-by-step design guideline of the robust PWM-SMC controller using the linearized model for

three-phase GCI with the *LCL* filter. The conclusions can be drawn as follows.

1) There are many ways to realize switching in the SMC system. The hysteresis modulator and pulsewidth modulator are the two special switching modes in the power electronics, which can ensure the switching of the system without extra nonlinear term in the control law.
2) Compared with the HM-SMC controller, the size of the output filter and the sampling frequency can be much smaller for the proposed strategy.
3) Different from the traditional PWM-SMC based on the Lyapunov stability or the phase plane, the proposed strategy has adopted the linear tool to design SMC parameters, where the accurate stability region can be exactly obtained, especially when the delay issue is addressed.

A 3-kW/3-phase/110-V experimental lab setup has been constructed to verify the feasibility of the proposed PWM-SMC controller using the linearized model design strategy. The experimental results show that the proposed PWM-SMC controller has excellent robustness against the filter parameters shift and satisfactory dynamic performance, even under the condition of a seriously distorted grid.

REFERENCES

[1] F. Blaabjerg, R. Teodorescu, M. Liserre, and A. V. Timbus, "Overview of control and grid synchronization for distributed power generation systems," *IEEE Trans. Ind. Electron.*, vol. 53, no. 5, pp. 1398–1409, Oct. 2006.

[2] W. Wu, Y. He, and F. Blaabjerg, "An *LLCL* power filter for single-phase grid-tied inverter," *IEEE Trans. Power Electron*," vol. 27, no. 2, pp. 782–789, Feb. 2012.

[3] R. Peña-Alzola, M. Liserre, F. Blaabjerg, R. Sebastián, J. Dannehl, and F.W. Fuchs, "Analysis of the passive damping losses in *LCL*-filter-based grid converters," *IEEE Trans. Power Electron.*, vol. 28, no. 6, pp. 2642–2646, Jun. 2013.

[4] W. Wu, Y. He, T. Tang, and F. Blaabjerg, "A new design method for the passive damped *LCL* and *LLCL* filter-based single-phase grid-tied inverter," *IEEE Trans. Ind. Electron.*, vol. 60, no. 10, pp. 4339–4350, Oct. 2013.

[5] Z. Bai, H. Ma, D. Xu, B. Wu, Y. Fang, and Y. Yao, "Resonance damping and harmonic suppression for grid-connected current-source converter," *IEEE Trans. Ind. Electron.*, vol. 61, no. 7, pp. 3146–3154, Jul. 2014.

[6] R. Peña-Alzola, M. Liserre, F. Blaabjerg, M. Ordonez, and T. Kerekes, "A self-commissioning notch filter for active damping in a three-phase LCL-filter-based grid-tie converter," *IEEE Trans. Power Electron.*, vol. 29, no. 12, pp. 6754–6761, Dec. 2014.

[7] Y. Liu, W. Wu, Y. He, Z. Lin, F. Blaabjerg, and H. S.-H. Chung, "An efficient and robust hybrid damper for *LCL*- or *LLCL*-based grid-tied inverter with strong grid-side harmonic voltage effect rejection," *IEEE Trans. Ind. Electron.*, vol. 63, no. 2, pp. 926–936, Feb. 2016.

[8] M. B. Saïd-Romdhane, M. W. Naouar, I. Slama-Belkhodja, and E. Monmasson, "Robust active damping methods for LCL filter-based grid-connected converters," *IEEE Trans. Power Electron.*, vol. 32, no. 9, pp. 6739–6750, Sep. 2017.

[9] W. Wu, Y. Liu, Y. He, H. S.-H. Chung, M. Liserre, and F. Blaabjerg, "Damping methods for resonances caused by LCL-filter-based current-controlled grid-tied power inverters: an overview," *IEEE Trans. Ind. Electron.*, vol. 64, no. 9, pp. 7402–7413, Sep. 2017.

[10] L. Jia, X. Ruan, W. Zhao, Z. Lin, and X. Wang, "An adaptive active damper for improving the stability of grid-connected inverters under weak grid," *IEEE Trans. Power Electron.*, vol. 33, no. 11, pp. 9561–9574, Nov. 2018.

[11] J. Roldán-Pérez, E. J. Bueno, R. Peña-Alzola, and A. Rodríguez-Cabero, "All-pass-filter-based active damping for VSCs with LCL filters connected to weak grids," *IEEE Trans. Power Electron.*, vol. 33, no. 11, pp. 9890–9901, Nov. 2018.

[12] Z. Zhang *et al.*, "Principle and robust impedance-based design of grid-tied inverter with LLCL-Filter under wide variation of grid-reactance," *IEEE Trans. Power Electron.*, vol. 34, no. 5, pp. 4362–4374, 2019.

[13] J. A. Rohten *et al.*, "Model predictive control for power converters in a distorted three-phase power supply," *IEEE Trans. Ind. Electron.*, vol. 63, no. 9, pp. 5838–5848, Sep. 2016.

[14] N. Panten, N. Hoffmann, and F. W. Fuchs, "Finite control set model predictive current control for grid-connected voltage-source converters with LCL filters: A study based on different state feedbacks," *IEEE Trans. Power Electron.*, vol. 31, no. 7, pp. 5189–5200, Jul. 2016.

[15] S. Bayhan, M. Trabelsi, H. Abu-Rub, and M. Malinowski, "Finite-control-set model-predictive control for a quasi-z-source four-leg inverter under unbalanced load condition," *IEEE Trans. Ind. Electron.*, vol. 64, no. 4, pp. 2560–2569, Apr. 2017.

[16] S. R. Mohapatra and V. Agarwal, "Model predictive controller with reduced complexity for grid-tied multilevel inverters," *IEEE Trans. Ind. Electron.*, vol. 66, no. 11, pp. 8851–8855, 2019.

[17] H. Komurcugil, N. Altin, S. Ozdemir, and I. Sefa, "Lyapunov-function and proportional-resonant-based control strategy for single-phase grid-connected VSI with LCL filter," *IEEE Trans. Ind. Electron.*, vol. 63, no. 5, pp. 2838–2849, May 2016.

[18] Y. Gui, B. Wei, M. Li, J. M. Guerrero, and J. C. Vasquez, "Passivity-based coordinated control for islanded AC microgrid," *Appl. Energy*, vol. 229, pp. 551–561, 2018.

[19] Y. Chen, M. Wen, E. Lei, X. Yin, J. Lai, and Z. Wang, "Passivity-based control of cascaded multilevel converter based D-STATCOM integrated with distribution transformer," *Electr. Power Syst. Res.*, vol. 154, pp. 1–12, Jan. 2018.

[20] X. Mu, J. Wang, W. Wu, and F. Blaabjerg, "A modified multifrequency passivity-based control for shunt active power filter with model-parameter-adaptive capability," *IEEE Trans. Ind. Electron.*, vol. 65, no. 1, pp. 760–769, Jan. 2018.

[21] M. Merai, M. W. Naouar, I. Slama-Belkhodja, and E. Monmasson, "An adaptive PI controller design for DC-link voltage control of single-phase grid-connected converters," *IEEE Trans. Ind. Electron.*, vol. 66, no. 8, pp. 6241–6249, 2019.

[22] Z.-X. Zou, G. Buticchi, and M. Liserre, "Grid identification and adaptive voltage control in a smart transformer-fed grid," *IEEE Trans. Power Electron.*, vol. 34, no. 3, pp. 2327–2338, 2019.

[23] D. Martin and E. Santi, "Autotuning of digital deadbeat current controllers for grid-tie inverters using wide bandwidth impedance identification," *IEEE Trans. Ind. Appl.*, vol. 50, no. 1, pp. 441–451, Jan./Feb. 2014.

[24] Y. He, H. S.-H. Chung, C. N.-M. Ho, and W. Wu, "Modified cascaded boundary-deadbeat control for a virtually-grounded three-phase grid-connected inverter with LCL filter," *IEEE Trans. Power Electron.*, vol. 32, no. 10, pp. 8163–8180, Oct. 2017.

[25] Y. He, H. S.-H. Chung, C. N.-M. Ho, and W. Wu, "Use of boundary control with second-order switching surface to reduce the system order for deadbeat controller in grid-connected inverter," *IEEE Trans. Power Electron.*, vol. 31, no. 3, pp. 2638–2653, Mar. 2016.

[26] H. Komurcugil, S. Ozdemir, I. Sefa, N. Altin, and O. Kukrer, "Sliding mode control for single-phase grid-connected LCL filtered VSI with double-band hysteresis scheme," *IEEE Trans. Ind. Electron.*, vol. 63, no. 2, pp. 864–873, Feb. 2016.

[27] R. Guzman, L. G. de Vicuña, M. Castilla, J. Miret, and J. de la Hoz, "Variable structure control for three-phase LCL-filtered inverters using a reduced converter model," *IEEE Trans. Ind. Electron.*, vol. 65, no. 1, pp. 5–15, Jan. 2018.

[28] R. Guzman, L. G. de Vicuña, M. Castilla, J. Miret, and H. Martín, "Variable structure control in natural frame for three-phase grid-connected inverters with LCL filter," *IEEE Trans. Power Electron.*, vol. 33, no. 5, pp. 4512–4522, May 2018.

[29] X. Hao, X. Yang, T. Liu, L. Huang, and W. Chen, "A sliding-mode controller with multiresonant sliding surface for single-phase grid-connected VSI with an LCL filter," *IEEE Trans. Power Electron.*, vol. 28, no. 5, pp. 2259–2268, May 2013.

[30] R. P. Vieira, L. T. Martins, J. R. Massing, and M. Stefanello, "Sliding mode controller in a multiloop framework for a grid-connected VSI with LCL filter," *IEEE Trans. Ind. Electron.*, vol. 65, no. 6, pp. 4714–4723, Jun. 2018.

[31] M. A. E. Alali, Y. B. Shtessel, and J.-P. Barbot, "Grid-connected shunt active LCL control via continuous sliding modes," *IEEE/ASME Trans. Mechatronics*, vol. 24, no. 2, pp. 729–740, Apr. 2019.

[32] J. Y. Hung, W. Gao, and J. C. Hung, "Variable structure control: A survey," *IEEE Trans. Ind. Electron.*, vol. 40, no. 1, pp. 2–22, Feb. 1993.

[33] W. Gao and J. C. Hung, "Variable structure control of nonlinear systems: A new approach," *IEEE Trans. Ind. Electron.*, vol. 40, no. 1, pp. 45–55, Feb. 1993.
[34] S.-C. Tan, Y. M. Lai, C. K. Tse, and M. K. H. Cheung, "A fixed-frequency pulsewidth modulation based quasi-sliding-mode controller for buck converters," *IEEE Trans. Power Electron.*, vol. 20, no. 6, pp. 1379–1392, Nov. 2005.
[35] S.-C. Tan, Y. M. Lai, C. K. Tse, L. Martinez-Salamero, and C. Wu, "A fast-response sliding-mode controller for boost-type converters with a wide range of operating conditions," *IEEE Trans. Ind. Electron.*, vol. 54, no. 6, pp. 3276–3286, Dec. 2007.
[36] A. Abrishamifar, A. Ahmad, and M. Mohamadian, "Fixed switching frequency sliding mode control for single-phase unipolar inverters," *IEEE Trans. Power Electron.*, vol. 27, no. 5, pp. 2507–2514, May 2012.
[37] D. Pan, X. Ruan, C. Bao, W. Li, and X. Wang, "Optimized controller design for LCL-type grid-connected inverter to achieve high robustness against grid-impedance variation," *IEEE Trans. Ind. Electron*, vol. 62, no. 3, pp. 1537–1547, Mar. 2015.

Han Li was born in Anhui Province, China, in 1995. He received the M.S. degree in electrical engineering from Shanghai Maritime University, Shanghai, China, in 2020.

His current research interests include the sliding-mode control, digital control techniques, and renewable energy generation systems.

Weimin Wu (Member, IEEE) received the Ph.D. degree in electrical engineering from the College of Electrical Engineering, Zhejiang University, Hangzhou, China, in 2005.

From July 2005 to June 2006, he was a Research Engineer with the Delta Power Electronic Center, Shanghai. Since July 2006, he has been a Faculty Member, Shanghai Maritime University, Shanghai, China, where he is currently a Full Professor with the Department of Electrical Engineering. He was a Visiting Professor with the Center for Power Electronics Systems, Virginia Polytechnic Institute and State University, Blacksburg, VA, USA, from September 2008 to March 2009. From November 2011 to January 2014, he was also a Visiting Professor with the Department of Energy Technology, Aalborg University, Aalborg, Demark, where he was with the Center of Reliable Power Electronics. He has coauthored more than 100 papers and holds 8 patents. His areas of interests include the power converters for renewable energy systems, power quality, smart grid, and energy storage technology.

Dr. Wu serves as an Associate Editor for the IEEE TRANSACTIONS ON INDUSTRY ELECTRONICS.

Min Huang received the M.S. degree in electrical engineering from Shanghai Maritime University, Shanghai, China, in 2012, and the Ph.D. degree from the Institute of Energy Technology, Aalborg University, Aalborg, Denmark, in 2015.

She is currently a Faculty Member with Shanghai Maritime University, Shanghai. Her research interests include power quality, control, and power converters for renewable energy systems.

Henry Shu-hung Chung (Fellow, IEEE) received the B.Eng. and Ph.D. degrees in electrical engineering from Hong Kong Polytechnic University, Hong Kong, in 1991 and 1994, respectively.

Since 1995, he has been with the City University of Hong Kong, Hong Kong, where he is currently a Chair Professor with the Department of Electrical Engineering and the Director of the Center for Smart Energy Conversion and Utilization Research. He has edited one book, authored eight research book chapters, and more than 460 technical papers, including 200 refereed journal papers in his research areas, and holds 50 patents. His current research interests include renewable energy conversion technologies, lighting technologies, smart grid technologies, and computational intelligence for power electronic systems.

Dr. Chung was a recipient of numerous industrial awards for his invented energy saving technologies. He was the Chair of the Technical Committee of the High-Performance and Emerging Technologies, IEEE Power Electronics Society from 2010 to 2014. He was an Editor-in-Chief for the IEEE *Power Electronics Letters* from 2014 to 2018. He is currently an Associate Editor for the IEEE TRANSACTIONS ON POWER ELECTRONICS and the IEEE JOURNAL OF EMERGING AND SELECTED TOPICS IN POWER ELECTRONICS.

Marco Liserre (Fellow, IEEE) received the M.Sc. and Ph.D. degrees in electrical engineering from the Polytechnic University of Bari, Bari, Italy, in 1998 and 2002, respectively.

He has been an Associate Professor with the Polytechnic University of Bari, Bari, and since 2012, a Professor of Reliable Power Electronics, Aalborg University, Aalborg, Denmark. Since 2013, he is currently a Full Professor and he holds the Chair of Power Electronics, Kiel University, Kiel, Germany. He has authored or coauthored 400 technical papers (more than one-third of them in international peer-reviewed journals) and a book. His works have received more than 28 000 citations. He is listed in ISI Thomson report "The world's most influential scientific minds" in 2014.

Dr. Liserre was a recipient of the IES 2009 Early Career Award, the IES 2011 Anthony J. Hornfeck Service Award, the 2014 Dr. Bimal Bose Energy Systems Award, the 2011 Industrial Electronics Magazine Best Paper Award, the Third Prize Paper Award by the Industrial Power Converter Committee, ECCE 2012, 2012 and 2017 IEEE PELS Sustainable Energy Systems Technical Achievement Award, the 2018 IEEE-IES Mittelmann Achievement Award, and an ERC Consolidator Grant for the project "The highly efficient and reliable smart transformer (HEART), a new heart for the electric distribution system." He is member of IAS, PELS, PES, and IES. He has been serving all these societies in different capacities.

Frede Blaabjerg (Fellow, IEEE) received the Ph.D. degree in electrical engineering from Aalborg University, Aalborg, Denmark, in 1995.

He was with ABB-Scandia, Randers, Denmark, from 1987 to 1988. He was an Assistant Professor in 1992, an Associate Professor in 1996, and a Full Professor of power electronics and drives in 1998. From 2017, he was a Villum Investigator. He is an Honoris Causa at University Politehnica Timisoara, Timisoara, Romania, and Tallinn Technical University, Tallinn, Estonia. He has authored or coauthored more than 600 journal papers in the fields of power electronics and its applications. He is the co-author of four monographs and editor for ten books in power electronics and its applications. His current research interests include power electronics and its applications such as in wind turbines, PV systems, reliability, harmonics and adjustable speed drives.

Dr. Blaabjerg was a recepient of 32 IEEE Prize Paper Awards, the IEEE PELS Distinguished Service Award in 2009, the EPE-PEMC Council Award in 2010, the IEEE William E. Newell Power Electronics Award 2014, the Villum Kann Rasmussen Research Award 2014, the Global Energy Prize in 2019, and the 2020 IEEE Edison Medal. He was the Editor-in-Chief for the IEEE TRANSACTIONS ON POWER ELECTRONICS from 2006 to 2012. He was a Distinguished Lecturer for the IEEE Power Electronics Society from 2005 to 2007 and for the IEEE Industry Applications Society from 2010 to 2011 as well as from 2017 to 2018. During 2019—2020, he serves as a President of the IEEE Power Electronics Society. He is the Vice-President of the Danish Academy of Technical Sciences too. He is nominated in 2014-2019 by Thomson Reuters to be between the most 250 cited researchers in Engineering in the world.